Theranostic near-infrared fluorescent nanoplatform for imaging and systemic siRNA delivery to metastatic anaplastic thyroid cancer

Yanlan Liu[a,1], Viswanath Gunda[b,1], Xi Zhu[a], Xiaoding Xu[a], Jun Wu[a], Diana Askhatova[a], Omid C. Farokhzad[a,2], Sareh Parangi[b,2], and Jinjun Shi[a,2]

[a]Department of Anesthesiology, Brigham and Women's Hospital, Harvard Medical School, Boston, MA 02115; and [b]Department of Surgery, Massachusetts General Hospital, Harvard Medical School, Boston, MA 02214

Edited by Mark E. Davis, California Institute of Technology, Pasadena, CA, and approved May 16, 2016 (received for review April 12, 2016)

Anaplastic thyroid cancer (ATC), one of the most aggressive solid tumors, is characterized by rapid tumor growth and severe metastasis to other organs. Owing to the lack of effective treatment options, ATC has a mortality rate of ∼100% and median survival of less than 5 months. RNAi nanotechnology represents a promising strategy for cancer therapy through nanoparticle (NP) -mediated delivery of RNAi agents (e.g., siRNA) to solid tumors for specific silencing of target genes driving growth and/or metastasis. Nevertheless, the clinical success of RNAi cancer nanotherapies remains elusive in large part because of the suboptimal systemic siRNA NP delivery to tumors and the fact that tumor heterogeneity produces variable NP accumulation and thus, therapeutic response. To address these challenges, we here present an innovative theranostic NP platform composed of a near-infrared (NIR) fluorescent polymer for effective in vivo siRNA delivery to ATC tumors and simultaneous tracking of the tumor accumulation by noninvasive NIR imaging. The NIR polymeric NPs are small (∼50 nm), show long blood circulation and high tumor accumulation, and facilitate tumor imaging. Systemic siRNA delivery using these NPs efficiently silences the expression of V-Raf murine sarcoma viral oncogene homolog B (BRAF) in tumor tissues and significantly suppresses tumor growth and metastasis in an orthotopic mouse model of ATC. These results suggest that this theranostic NP system could become an effective tool for NIR imaging-guided siRNA delivery for personalized treatment of advanced malignancies.

theranostic | nanoparticle | NIR imaging | siRNA delivery | anaplastic thyroid cancer

Thyroid cancer has been continuously increasing in worldwide incidence for the past few decades and is now the fifth most common malignancy in females (1). Notably, the most aggressive form of thyroid cancer, anaplastic thyroid cancer (ATC), has a mortality rate of nearly 100%, with median survival time of 3–5 months, mainly because of local invasion and metastasis to lung, lymph nodes (LNs), and other tissues (2). The mechanisms that mediate metastasis in ATC strongly depend on the activation of genetic mutations, such as V-Raf murine sarcoma viral oncogene homolog B (BRAF), TP53, RAS, PIK3CA, and AKT1 (3). Current treatments for ATC rely on various combinations of surgical resection with adjuvant therapies, such as chemotherapy and radiotherapy, but have shown only limited survival benefits (4). Therefore, there are compelling reasons to establish new strategies for more effective treatment of metastatic ATC.

RNAi is a powerful means for specific silencing of virtually any target gene of interest, thus offering an enormous opportunity to treat cancers and suppress metastases (5). By improving the in vivo delivery of RNAi agents (e.g., siRNA) to solid tumor tissues through the enhanced permeability and retention (EPR) effect (6), nanotechnology has drastically facilitated the clinical translation of RNAi for cancer therapy (5). However, RNAi nanoparticles (NPs) at the clinical stage for cancer treatment (7, 8) may still face challenging obstacles, such as suboptimal systemic delivery of siRNA into target tumor cells. In addition, it has been increasingly recognized that the EPR effect varies substantially among both patients and tumor types and even within the same patient/tumor type over time (9), representing another important challenge for RNAi nanotherapeutics to identify patients most likely to benefit from them. The heterogeneous response of cancer nanomedicines in clinical trials has recently prompted the need to incorporate imaging modalities to identify cancer patients with stronger EPR effects and NP accumulation (10, 11). By integrating diagnostic and therapeutic functions into a single NP formulation, theranostic nanomedicine offers a promising strategy to monitor the therapeutic pharmacokinetics and accumulation and the pathological process longitudinally, yielding important insights into tumor heterogeneities and EPR for patient selection and predictive nanomedicine (12). It is also worth noting that time is usually of the essence for treatment of ATC because of the unique rapid nature of the disease progression and the development of massive local invasion and distant metastases. Thus, a theranostic approach allows rapid visualization and treatment simultaneously with a targeted therapy, the delivery and efficacy of which are otherwise hard to determine.

Herein, we develop an innovative theranostic NP platform using a near-infrared (NIR) fluorescent polymer for effective in vivo siRNA delivery and noninvasive NIR imaging to monitor whole-body biodistribution kinetics and tumor localization of

Significance

Current therapies have shown limited success in improving outcomes for lethal anaplastic thyroid cancer (ATC) characterized by rapid tumor growth and metastatic dissemination caused by the activation of genetic mutations. RNAi nanotechnology is emerging as a promising strategy for effectively treating such cancers and suppressing metastasis. However, suboptimal systemic delivery of RNAi agents to tumors and variable therapeutic responses because of tumor heterogeneity represent challenging hurdles to widespread clinical use. We describe an innovative near-infrared nanoplatform for systemic delivery of siRNA to ATC and real-time tracking of tumor accumulation. Antitumor growth and antimetastasis effects in an orthotopic ATC mouse model suggest this nanoplatform as a valuable tool for personalized treatment of ATC and other advanced malignancies.

Author contributions: Y.L., V.G., O.C.F., S.P., and J.S. designed research; Y.L., V.G., X.Z., X.X., J.W., and D.A. performed research; Y.L., V.G., X.Z., X.X., J.W., O.C.F., S.P., and J.S. analyzed data; and Y.L., V.G., O.C.F., S.P., and J.S. wrote the paper.

Conflict of interest statement: O.C.F. discloses financial interest in BIND Therapeutics, Selecta Biosciences, and Tarveda Therapeutics.

This article is a PNAS Direct Submission.

[1]Y.L. and V.G. contributed equally to this work.

[2]To whom correspondence may be addressed. Email: jshi@bwh.harvard.edu, sparangi@partners.org, or ofarokhzad@bwh.harvard.edu.

This article contains supporting information online at www.pnas.org/lookup/suppl/doi:10.1073/pnas.1605841113/-/DCSupplemental.

siRNA NPs after systemic administration. Compared with common axial imaging techniques, noninvasive NIR imaging is considered both safer and more potent because of its higher sensitivity, improved resolution, and nonionizing radiation (13). In addition, the anatomical position of the thyroid gland makes NIR imaging very attractive in tracking the accumulation of siRNA NPs in ATC tumors. We show that these small theranostic polymeric NPs (~50 nm) with high photostability and long systemic circulation times possess several properties favorable for treatment of ATC: (*i*) in situ tumor imaging of EPR-mediated NP accumulation, (*ii*) noninvasive LN imaging with the potential to improve precision in surgery and cancer staging, (*iii*) effective protection and delivery of siRNA into tumors, (*iv*) significant inhibition of tumor growth in both xenograft and more clinically relevant orthotopic models of ATC, (*v*) dramatic reduction of micrometastases in lung, and (*vi*) negligible adverse effects and systemic inflammatory responses. It is also worth noting that this is the first example, to our knowledge, of NP-mediated systemic delivery of siRNA to ATC, which is nearly uniformly lethal with current therapeutic regimens. We expect this study to pave the way for the development of NIR NP platforms for imaging-guided siRNA delivery to advanced malignancies.

Results

Synthesis and Characterization of NIR NPs. Conjugated polymers are emerging as a unique class of optically and electronically active materials. The optical properties of these polymers, with fluorescent emission that is "tunable" from UV to NIR simply by varying the functional groups in the polymer backbone/side chain, have attracted interest in using them in diverse biomedical applications (14). Unlike traditional NIR semiconducting quantum dots, these polymers do not pose the danger of metal-induced toxicity to living organisms. Herein, we describe selecting poly[2,6-(4,4-bis-(2-ethylhexyl)-4H-cyclopenta [2,1-b;3,4-b′]dithiophene)-alt-4,7(2,1,3-benzothiadiazole)] (polyPCPDTBT) with both excitation and emission in the NIR region as the building block for our NP polymeric platform for NIR imaging and siRNA delivery (Fig. 1*A*). Because the high hydrophobicity of polyPCPDTBT also enables effective hydrophobic interaction with the amphiphilic cationic lipids that are widely used for complexing with siRNA, the NIR RNAi NPs can be formulated through a modified self-assembly nanoprecipitation method that we recently developed (15), with an siRNA encapsulation efficiency of ~50%. With a surface coating of 1,2-distearoyl-*sn*-glycero-3-phosphoethanolamine-*N*-[methoxy(polyethylene glycol)], the resulting NPs were highly dispersed in the aqueous solution and remained stable within 1 month. Fig. 1*B* shows the excitation/emission spectrum of the NIR NPs; under irradiation of 710 nm light, the NPs exhibited bright NIR imaging fluorescence (*SI Appendix*, Fig. S1*A*). A typical transmission electron microscopy (TEM) image in Fig. 1*C* illustrates that these NPs were spherical in shape, with an average diameter of ~50 nm and a hydrodynamic size of ~85 nm (*SI Appendix*, Fig. S1*B*).

To assess the gene silencing efficiency of the NPs, we first studied the cellular internalization of the NIR NPs loaded with DY547-labeled siRNA in HeLa cells. The red fluorescence observed in the cytoplasm of NP-treated cells indicates the intracellular siRNA delivery (Fig. 1*D*). By monitoring the changes in fluorescence intensity after incubation of NPs with HeLa cells pretreated with different inhibitors (16), it was confirmed that clathrin-mediated endocytosis and micropinocytosis were responsible for the internalization of the majority of NPs (*SI Appendix*, Fig. S2 *A* and *B*) (17). Next, we studied the effect of NP surface charge on gene silencing by encapsulating luciferase siRNA into three different NIR NPs (NP#1, NP#2, and NP#3) with different ζ-potentials (Fig. 1*E*). Using LysoTracker for labeling endosomes of the cells, we found that siRNA encapsulated in these NPs escaped from the endosome into the cytoplasm where the RNAi machinery resides (*SI Appendix*, Fig. S2*C*) (18). Moreover, all of the NPs showed sustained siRNA release, and no apparent differences were found during incubation (*SI Appendix*, Fig. S3). Silencing efficacy was then assessed using luciferase-expressing HeLa cells. As shown in Fig. 1 *F*–*H*, all NPs achieved dose-dependent silencing of luciferase with over 90% knockdown at a concentration of 50 nM without obvious cytotoxicity. However, at lower concentrations, NP#3 was much more potent than either NP#1 or NP#2 because of the positive charges on its surface, which efficiently interacted with the negative membrane surface of cells, promoting the internalization of NP#3 more than the other two formulations (*SI Appendix*, Fig. S4).

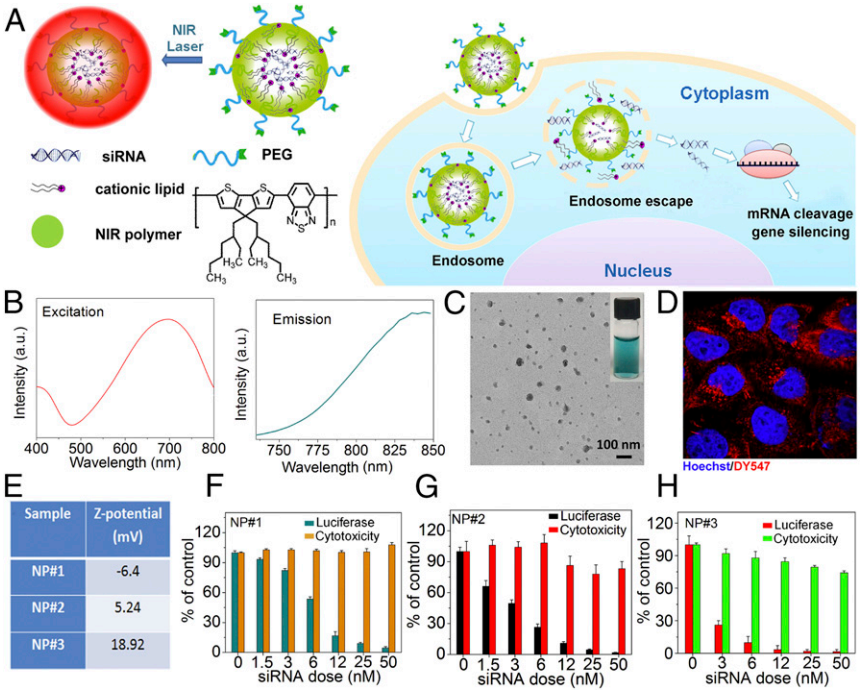

Fig. 1. NIR NP platform. (*A*) Schematic illustration of the NIR NPs for siRNA delivery. (*B*) Excitation and emission of NIR NPs. (*C*) The TEM image of the NIR NPs. *Inset* is the digital picture of the NIR NPs in PBS. (*D*) Confocal imaging of HeLa cells incubated with the NIR NPs loaded with DY547-labeled siRNA. (*E*) ζ-Potentials of three different NIR NPs loaded with luciferase siRNA (NP#1, NP#2, and NP#3). Silencing efficiency and cytotoxicity of (*F*) NP#1, (*G*) NP#2, and (*H*) NP#3 loaded with luciferase siRNA.

In Vivo NIR Imaging. To assess the potential of the NPs for effective NIR imaging, we first tested their photostability, an important factor for optical imaging. The fluorescence intensity of the NIR NPs remained constant within 2 h of strong laser exposure, and only ∼14% decay was observed after 12 h (*SI Appendix*, Fig. S5). Next, we examined the pharmacokinetics of the NIR NPs, because a long circulation half-life is essential for tumor accumulation of nanotherapeutics by the EPR effect (19). Three NIR NPs with different surface charges were i.v. injected into healthy mice, and blood was withdrawn at the indicated time points for the measurement of NP fluorescence. All three NP formulations displayed long circulation time (Fig. 2*A*), which was prolonged with decreased ζ-potential, presumably attributable to the lower uptake of NPs by the mononuclear phagocytic system (20). Specifically, the NPs with negative surface charge (NP#1) showed the longest half-life, with ∼40% of NPs remaining in the blood 24 h postinjection. Given the potential immunogenic response associated with NPs with highly positive charges (21), we selected the NP formulation with a lower positive charge but a favorable in vitro silencing effect (NP#2) for the following in vivo experiments unless otherwise specified.

After i.v. injection of a single dose of NPs, time-dependent whole-body NIR fluorescence images were collected (Fig. 2*B*). Their long circulation time allowed these NPs to be only gradually cleared from the blood and had a greater tendency to accumulate in the tumor with time. After 24 h, the tumor-bearing mouse was killed, and the organs were collected for quantification analysis (Fig. 2*C*). The tumor showed strong NIR fluorescence, and the fluorescence intensity per tissue area for tumor was even comparable with that of liver (*SI Appendix*, Fig. S6). To further clarify the potential of NIR NPs in visualizing the EPR effect, mice bearing orthotropic 8505C ATC tumors were i.v. injected with NIR NPs, and the accumulation of NIR NPs was investigated. Impressively, high-level accumulation of NIR NPs in the tumor was also observed without excision (*SI Appendix*, Fig. S7), indicating the great potential of NIR NPs as a marker for real-time prediction of EPR-mediated tumor accumulation of siRNA-loaded NPs in different cancer patients through noninvasive NIR imaging. In addition, the large blood vessels can be clearly visualized even after 4 h postinjection, and the tumor tissues can be clearly differentiated from adjacent tissues under NIR irradiation. Notably, the adequate contrast between vessels and surrounding tissues as well as between tumors and normal tissues provided by the NIR NPs could also aid surgeons by clarifying anatomic considerations, such as margins, and establishing the proximity and involvement of nearby vessels.

In addition to tumors, NIR imaging is also emerging as an effective medical option for guidance in finding LNs in a less invasive way for accurately staging cancer and assessing the metastatic progress, a process called sentinel lymph node (SLN) mapping (22). After s.c. injection of the NPs into mouse forepaws, strong NIR fluorescence from the axillary LNs was detected within 10 min without the need for any surgical incision (Fig. 2*E*), indicating that NPs have migrated to the LNs through lymphatic drainage. Furthermore, 24 h after tail vein injection, the NIR NPs also efficiently accumulated in the axillary, inguinal, lateral thoracic, and neck LNs (Fig. 2*D*). These findings indicate that these NPs may also be useful for NIR imaging-guided LN removal.

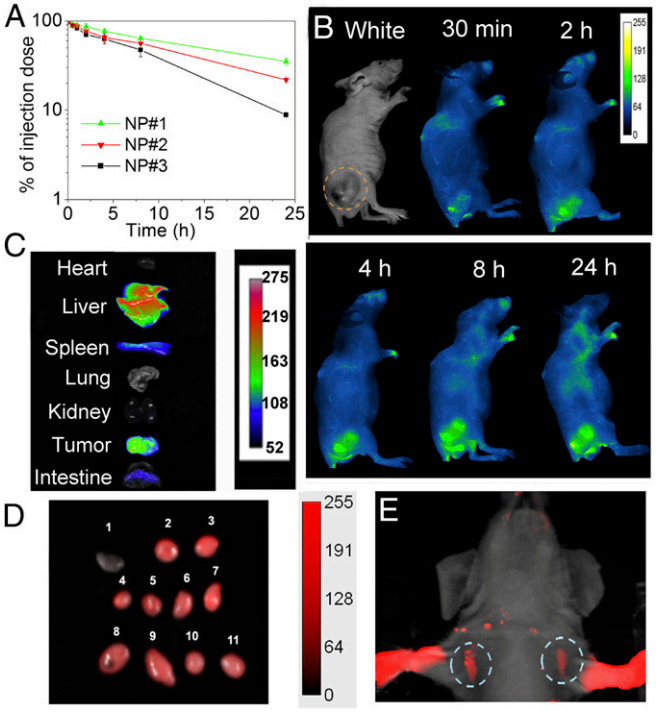

Fig. 2. In vivo NIR imaging. (*A*) Pharmacokinetics profile of NP#1, NP#2, and NP#3. (*B*) Time-dependent fluorescence imaging of a $BRAF^{V600E}$-mutated 8505C tumor-bearing mouse after a single-dose injection of NIR NPs. (*C*) NIR fluorescence images of organs from *B*. (*D*) NIR fluorescence imaging of LNs at 24 h after i.v. injection of NIR NPs: 1, a small piece of muscle; 2 and 3, inguinal LNs; 4–7, neck LNs; 8 and 9, lateral thoracic LNs; and 10 and 11, axillary LNs. (*E*) SLN mapping 10 min after s.c. injection of NIR NPs into the forepaws.

In Vitro and in Vivo BRAF Silencing in ATC. Activation and up-regulation of BRAF by several mutations, such as the T1799A (V600E) point mutation that occurs in exon 15, have been recently confirmed in patients with ATC. This mutation results in overactivation of the MAPK pathway as evidenced by constitutive activation of the downstream mitogen-activated protein kinase kinase (MEK) and extracellular signal-regulated kinase (ERK) and subsequent cellular proliferation, invasion, angiogenesis, metastasis, and dedifferentiation, which ultimately result in radioactive iodine refractoriness and tumor recurrence (23, 24). Thus, the feasibility of using the NIR NPs to deliver siRNA targeting BRAF (siBRAF) (*SI Appendix*, Table S1) in ATC was studied. As shown in Fig. 3 *A* and *B*, treatment of NP(siBRAF) efficiently knocked down the expression of BRAF in $BRAF^{V600E}$-mutated 8505C cells. Moreover, the knockdown of BRAF was accompanied by significant down-regulation of the expression of phospho-MEK and phospho-ERK1/2 downstream of $BRAF^{V600E}$ kinase activity without any effect on the expression of either total ERK1/2 or total MEK.

Next, the ability of NP(siBRAF) to inhibit 8505C proliferation was evaluated (Fig. 3*C* and *SI Appendix*, Fig. S8). Clearly, the proliferation of cells treated with NP(siBRAF) was drastically slowed compared with both nontreated cells and NP(siControl)-treated cells during the same period. The down-regulation of $BRAF^{V600E}$ mutation was also investigated to determine whether it inhibited the aggressive invasion and migratory capacity of 8505C cells (Fig. 3 *D* and *E*, and *SI Appendix*, Fig. S9*A*). With the treatment of NP(siControl), cells exhibited a strong capacity to spread into or transmigrate across the matrigel. When treated with NP(siBRAF), the numbers of invaded and migrated cells relative to the control groups were reduced over 5- and 15-fold, respectively, indicating a strong positive link between $BRAF^{V600E}$ mutation and the metastasis of 8505C cells. Similar results were obtained for another ATC cell line (SW1736) and the papillary thyroid cancer cell line (BCPAP) (*SI Appendix*, Fig. S9*B*). A more careful look at the images reveals fewer invaded BCPAP cells in the matrigel compared with 8505C and SW1736 cells, suggesting that the behavior of papillary thyroid cancer is much less aggressive than that of ATC. Attachment to the wall of the blood or lymph vessel is a critical step in the spread of cancer cells to new parts of the body.

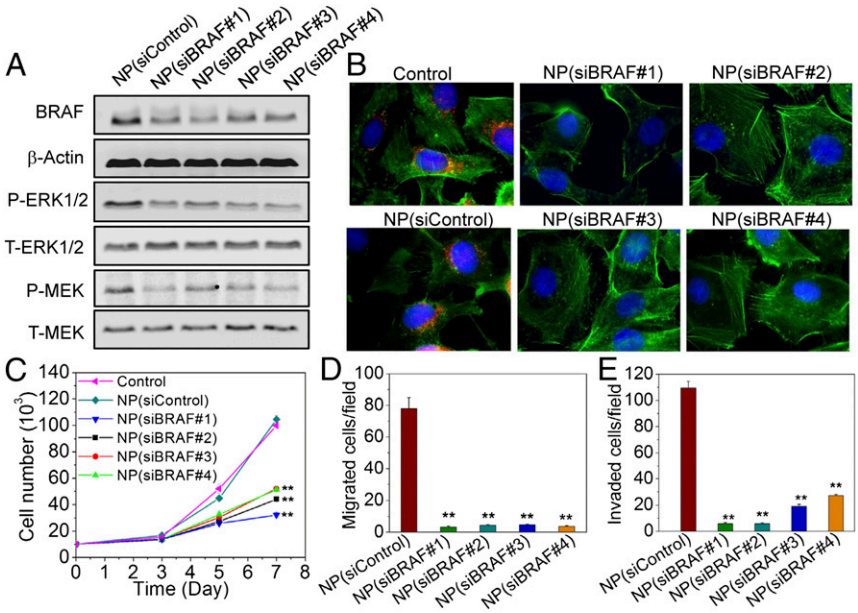

Fig. 3. NP-mediated BRAF silencing and functional effects in $BRAF^{V600E}$-mutated 8505C cells. (*A*) Western blot analysis of BRAF, total ERK1/2 (T-ERK1/2), phosphorylated ERK1/2 (P-ERK1/2), total MEK (T-MEK), and phosphorylated MEK (P-MEK) after treatment of NP(siControl) or NP(siBRAF) with different siBRAF sequences. (*B*) Immunofluorescence images of $BRAF^{V600E}$-mutated 8505C cells after treatment of NP(siControl) or NP(siBRAF) with different siBRAF sequences (red, BRAF; green, actin; and blue, nucleus). (*C*) Cell proliferation of $BRAF^{V600E}$-mutated 8505C cells after treatment with NP(siControl) or NP(siBRAF) having different siBRAF sequences. (*D* and *E*) Migrated and invaded numbers of $BRAF^{V600E}$-mutated 8505C cells after treatment with NP(siControl) or NP(siBRAF) with different siBRAF sequences, respectively. $^{**}P < 0.01$ vs. NP(siControl).

$BRAF^{V600E}$-silenced 8505C cells also displayed a reduced potential to adhere to collagen-coated plates (*SI Appendix*, Fig. S10). Collectively, these findings support the potential of NP-mediated $BRAF^{V600E}$ silencing in the inhibition of tumor cell growth, invasion, and metastasis.

Given the in vitro results, we then examined whether NP(siBRAF) delivery to tumors could silence BRAF expression in tumor tissue, inhibit tumor growth, and prevent metastasis. Mice bearing $BRAF^{V600E}$-mutated 8505C xenograft tumors were subjected to i.v. administration of NP(siBRAF) for 3 d at a daily siRNA dose of 600 μg/kg. Twenty-four hours after the final injection, Western blot analysis was conducted to measure BRAF expression in the tumors. Compared with NP(siControl), NP(siBRAF) showed ∼60% down-regulation of BRAF protein expression, which was further evidenced by immunohistochemical (IHC) staining (Fig. 4 *A* and *B*). Tumor size was monitored every other day after NP (siRNA) treatment, showing that growth was significantly delayed compared with that in the PBS or NP(siControl) groups (Fig. 4 *C* and *D*). In addition, mice treated with NP(siBRAF) or NP(siControl) did not behave differently from control group mice in terms of eating, drinking, grooming, activity, urination, exploratory behavior, or neurological status. The body weights of both NP(siBRAF)- and NP(siControl)-treated groups gradually increased in a manner similar to that of the control group (Fig. 4*E*).

Antitumor and Antimetastasis Effects in the Orthotopic ATC Model. With the promising results obtained in the xenograft model, we extended in vivo studies to the orthotopic ATC model. The aggressive orthotopic tumor model has been widely accepted as a more clinically relevant and better predictive model to assess the anticancer therapeutic efficacy of drug delivery systems based on the fact that tumor cells are implanted directly into the target organ, providing a tumor microenvironment with biological, invasive, and metastatic properties more similar to clinical cases (25). To further explore the potential applications of our NPs in ATC treatment, we conducted in vivo studies using an orthotopic model of ATC by injecting $BRAF^{V600E}$-mutated 8505C cells directly into the thyroid of immunodeficiency SCID mice (26). All mice developed cancers with high proliferation and aggressive behavior similar to human ATC. Similar to the case in xenograft models, greater down-regulation of BRAF protein relative to NP(siControl) was also achieved after three daily injections of NP(siBRAF) (Fig. 5 *A*–*C*). During the 1-month observation, NP(siControl) treatment did not impede the growth of tumors. Impressively, the average tumor size for NP(siBRAF)-treated mice was ∼threefold smaller than those of the control groups (Fig. 5*D* and *SI Appendix*, Fig. S11). The expression of Ki67, a cellular marker for proliferation, in the tumors of NP(siBRAF)-treated mice was dramatically lower than that the control group as evidenced by IHC staining (*SI Appendix*, Fig. S12).

ATC is one of the most lethal human tumors, with rapid progression of the tumor both locally and at the sites of metastases. The rapid progress at the metastatic sites often leads to general cachexia and difficulty with breathing because of the presence of lung metastases, and many patients die because of massive metastatic load (4). Any treatment that can effectively reduce both local infiltration and metastatic progression would be most welcome. Similar to clinical observation, orthotopic ATC mice used in this study start showing micrometastasis as soon as 1 wk and increase in number very rapidly toward the end of 4 wk. To assess the antimetastatic capacity of our siRNA NPs, we used GFP-expressed 8505C cells harboring $BRAF^{V600E}$ for tumor implantation in the orthotopic tumor model. The mice were killed 1 month after tumor cell injection to the thyroid gland, and the GFP signals from lungs, the most common metastatic location from aggressive ATC, were measured. Although treatment of NP(siBRAF) did not completely inhibit the tumor metastasis, there were considerably fewer micrometastases in NP(siBRAF)-treated mice than in NP(siControl) mice (Fig. 5*E*). IHC staining results also showed less BRAF expression in the lungs of mice treated with NP(siBRAF) (*SI Appendix*, Fig. S13). Our results showing the efficient decrease of the micrometastases in the treated group with NP(siBRAF) can reinforce the clinical relevance of these particles in treating aggressive ATC in patients.

Systemic Toxicity. The potential side effects of the NIR NPs were also evaluated in vivo. Healthy C57BL/6 mice ($n = 4$) were i.v. administered free siBRAF, NP(siControl), or NP(siBRAF) by tail vein injection, and blood was collected for blood biochemistry. Six crucial hepatic indicators (alanine aminotransferase, aspartate aminotransferase, alkaline phosphatase, blood urine nitrogen, total protein, and albumin) were similar in the NP-treated groups and the control groups (*SI Appendix*, Fig. S14 *A*–*F*). In addition, we did not observe obvious hemolysis after incubation of complete blood samples with the NPs at tested concentrations, suggesting good blood compatibility (*SI Appendix*, Fig.

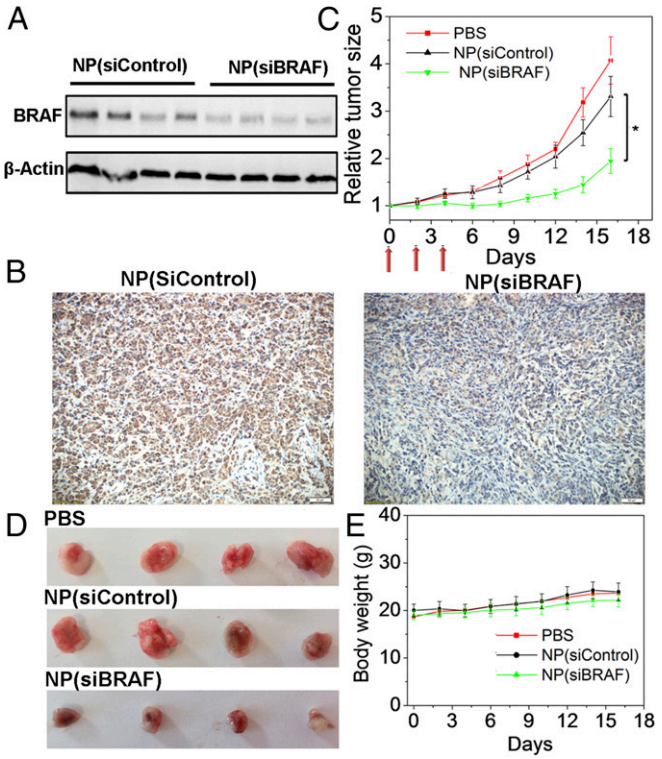

Fig. 4. In vivo antitumor effect of NP(siBRAF) in xenograft ATC mouse models. (*A*) Western blot analysis of BRAF expression in $BRAF^{V600E}$-mutated 8505C tumor tissue after systemic treatment with NP(siControl) and NP(siBRAF). (*B*) Immunochemical microphotographs of BRAF expression in $BRAF^{V600E}$-mutated 8505C tumor tissue after systemic treatment with NP(siControl) or NP(siBRAF). (*C*) Tumor growth curves of PBS-, NP(siControl)-, and NP(siBRAF)-treated $BRAF^{V600E}$-mutated 8505C tumor-bearing mice. Three i.v. injections are indicated by arrows. $*P < 0.05$ vs. NP(siControl). (*D*) Representative picture of tumors from *C*. (*E*) Body weight changes of three groups.

S14 *G* and *H*). No tissue damage or any other inflammatory response in the major organs was found in any experimental group as assessed by H&E staining (*SI Appendix*, Fig. S15). In addition, given that the induction of type I interferon (IFN) and inflammatory cytokines has been cited as a major concern in systemic siRNAs delivery, we further investigated the immunostimulatory effect of these NPs in immunocompetent mice through analyzing the levels of several cytokines in the blood after i.v. injection of therapeutic doses. Encouragingly, these NPs did not induce obvious elevation in the levels of serum IFN and inflammatory cytokines, including IFN-γ, IL-6, IL-12, and TNF-α (*SI Appendix*, Fig. S16).

Discussion

Conventional treatment strategies for ATC, one of the most aggressive solid tumors, assume that maximum patient benefit is achieved through complete surgical resection combined with adjuvant therapies, but most patients present late and are unresectable (4). RNAi NP-mediated silencing of genetic mutations that drive rapid tumor growth and metastasis has been emerging as an effective strategy for the treatment of advanced malignancies. However, the use of NPs for systemic siRNA delivery to ATC tumors has never been explored. In addition, to predict patient responses to siRNA nanotherapeutics and make this option clinically viable, it is necessary to understand their in vivo distribution in individual cancer patients with substantial variation in EPR, a critical mechanism that mediates tumor accumulation of nanomedicines.

Here, we show an innovative theranostic NIR NP platform for effective in vivo siRNA delivery to metastatic ATC tumors while simultaneously tracking tumor accumulation through noninvasive NIR imaging. Different from previous theranostic RNAi NPs, a commercially available and cost-effective conjugated NIR fluorescent polymer is used as the imaging agent and the carrier of siRNA, which avoids severe toxicity, multistep and complicated syntheses and purification, poor photostability, and negative effects on siRNA therapeutic activity, the key limitations of inorganic NIR fluorescent NPs or NIR dyes conjugated on siRNA or NPs that are typically used for imaging and tracking. Moreover, our NIR NPs are small and capable of both long circulation and high tumor accumulation in both xenograft and orthotopic ATC models. Its incorporation of noninvasive NIR imaging makes our NP platform a suitable tool for studying the fundamental questions regarding in vivo behavior of siRNA nanotherapies in different cancer patients, such that either the type or extent of the intervention can be individualized. In addition, we also noted strong NIR

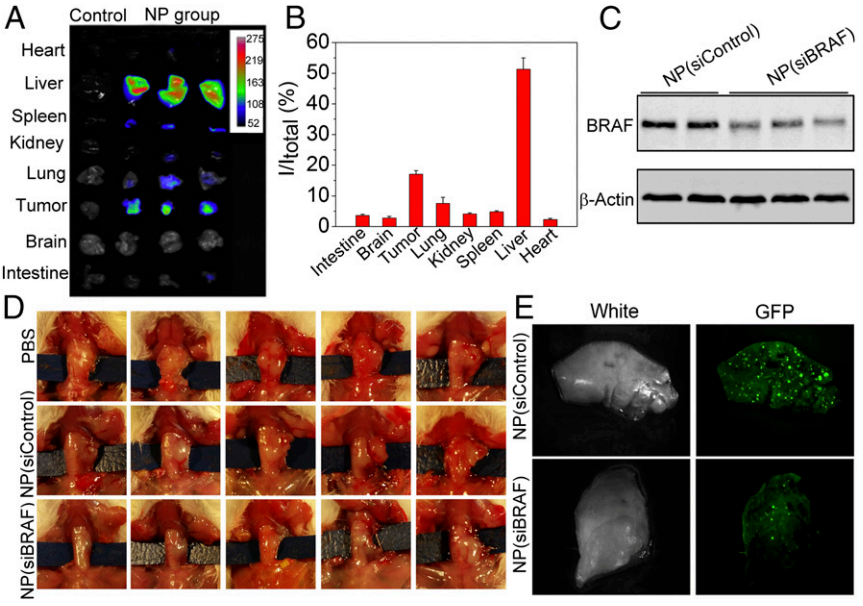

Fig. 5. In vivo inhibition of tumor growth and metastasis in the orthotopic ATC mouse model. (*A*) In vivo NIR imaging of different organs from nontreated and NP-treated mice (24 h after i.v. injection). (*B*) Biodistribution of NIR NPs quantified from *A*. (*C*) Western blot analysis of the BRAF expression in orthotopic ATC tumors after treatment with NP(siControl) or NP(siBRAF). (*D*) Therapeutic efficacy of NP(siBRAF) in orthotopic ATC mouse models. (*E*) Gross lung images from the mice bearing orthotopic ATC tumors with NP(siControl) or NP(siBRAF) treatment 1 month after injection with $BRAF^{V600E}$-mutated 8505C cells with GFP expression. Bright green spots indicate micrometastases.

fluorescence from different LNs under NIR irradiation after systemic or s.c. NP injection. Because LNs are struck earliest by almost all cancers, SLN mapping has been considered preferable to traditional dissection methods in assessing cancer progress and minimizing the spread of cancer not only before and after but also, during a treatment regimen. Contrast agents currently used in the clinic for SLN mapping are based on radioactive tracers or visible blue dyes (27). However, radioactive tracers are expensive and expose patients to ionizing radiation, while the blue dyes are invisible below the surface of tissues and stain the surgical field with poor contrast. The merits of NIR light (700–900 nm), such as the absence of ionizing radiation, high sensitivity, and deep tissue penetration, make the use of long-circulating NIR NPs presented here more attractive for SLN mapping.

BRAF mutation happens in ∼40% of ATC patients and has been associated with tumor growth, aggressiveness, and development of drug resistance. Moreover, other MAPK pathway genes (downstream of BRAF) account for another 20–40% of ATC cases (28), making BRAF an attractive target for ATC treatment. Surprisingly, RNAi therapy targeting BRAF has been rarely investigated in ATC, and no study has reported systemic delivery of BRAF siRNA NPs into ATC. Our findings show that the NIR NP platform can facilitate the in vivo delivery of siBRAF into ATC xenograft tumors, eliciting robust BRAF silencing in the tumor tissue and effective suppression of tumor growth without obvious side effects. Although several small molecule inhibitors of BRAF have recently been approved by the Food and Drug Administration for the treatment of late-stage melanoma with BRAF mutation, a phase II trial in patients with ATC has shown that the BRAF inhibitor sorafenib only modestly extends overall survival and allows relapse (29), largely because of the inevitable drug resistance. In addition, because of the need for long-term administration of inhibitors, patients often develop significant side effects, such as arthralgia, skin rash, and photosensitivity. We expect that the specific down-regulation of BRAF expression by RNAi NPs could provide an additional option in the treatment of lethal ATC.

Another important point of potential clinical benefit relates to the orthotopic ATC tumor model that we used in this study. Human ATC cells were orthotopically implanted into the thyroid, reproducing the real organ environment in which the tumor grows and facilitating metastatic spread of the resultant "primary" ATC tumors. With this model, we have been able to evaluate the antitumor and antimetastatic properties of siBRAF-loaded NIR NPs. Our results have shown that siBRAF-loaded NIR NPs dramatically slowed primary tumor growth, similar to the results obtained in the xenograft model. More impressively, systemic treatment with siBRAF-loaded NIR NPs significantly reduced the number of micrometastases in the lung. In conclusion, these findings highly facilitate the use of this nanoplatform as a robust siRNA delivery and tracking vehicle for efficient treatment of lethal ATC and other poor prognosis human diseases.

Materials and Methods

Methods and materials are provided in *SI Appendix*, including synthesis and characterization of NIR NPs; photostability of NPs; siRNA release kinetics; NP cellular uptake and endosomal escape; IHC staining; in vitro cell proliferation, invasion, and adhesion studies; and in vivo biodistribution, therapeutic efficacy, and NP toxicity studies. All animal experiments were approved by the Institutional Animal Care and Use Committee at Harvard Medical School.

ACKNOWLEDGMENTS. This work was supported by NIH Grants R00CA160350 (to J.S.), CA200900 (to J.S.), CA149738 (to S.P.), EB015419 (to O.C.F.), and U54-CA151884 (to O.C.F.); the Department of Defense Prostate Cancer Research Program Synergistic Idea Development Award (to O.C.F. and J.S.); the Movember–Prostate Cancer Foundation (PCF) Challenge Award (to O.C.F. and J.S.); the PCF Young Investigator Award (to J.S.); the Koch PCF Program in Nanotherapeutics (O.C.F.); and National Research Foundation of Korea Grant K1A1A2048701 (to O.C.F.).

1. Pellegriti G, Frasca F, Regalbuto C, Squatrito S, Vigneri R (2013) Worldwide increasing incidence of thyroid cancer: Update on epidemiology and risk factors. *J Cancer Epidemiol* 2013:965212.
2. Smallridge RC, et al.; American Thyroid Association Anaplastic Thyroid Cancer Guidelines Taskforce (2012) American Thyroid Association guidelines for management of patients with anaplastic thyroid cancer. *Thyroid* 22(11):1104–1139.
3. Xing M (2013) Molecular pathogenesis and mechanisms of thyroid cancer. *Nat Rev Cancer* 13(3):184–199.
4. Kebebew E, Greenspan FS, Clark OH, Woeber KA, McMillan A (2005) Anaplastic thyroid carcinoma. Treatment outcome and prognostic factors. *Cancer* 103(7):1330–1335.
5. Zuckerman JE, Davis ME (2015) Clinical experiences with systemically administered siRNA-based therapeutics in cancer. *Nat Rev Drug Discov* 14(12):843–856.
6. Maeda H, Nakamura H, Fang J (2013) The EPR effect for macromolecular drug delivery to solid tumors: Improvement of tumor uptake, lowering of systemic toxicity, and distinct tumor imaging in vivo. *Adv Drug Deliv Rev* 65(1):71–79.
7. Tabernero J, et al. (2013) First-in-humans trial of an RNA interference therapeutic targeting VEGF and KSP in cancer patients with liver involvement. *Cancer Discov* 3(4):406–417.
8. Zuckerman JE, et al. (2014) Correlating animal and human phase Ia/Ib clinical data with CALAA-01, a targeted, polymer-based nanoparticle containing siRNA. *Proc Natl Acad Sci USA* 111(31):11449–11454.
9. Prabhakar U, et al. (2013) Challenges and key considerations of the enhanced permeability and retention effect for nanomedicine drug delivery in oncology. *Cancer Res* 73(8):2412–2417.
10. Miller MA, et al. (2015) Predicting therapeutic nanomedicine efficacy using a companion magnetic resonance imaging nanoparticle. *Sci Transl Med* 7(314):314ra183.
11. Arrieta O, et al. (2014) High liposomal doxorubicin tumour tissue distribution, as determined by radiopharmaceutical labelling with (^{99m})Tc-LD, is associated with the response and survival of patients with unresectable pleural mesothelioma treated with a combination of liposomal doxorubicin and cisplatin. *Cancer Chemother Pharmacol* 74(1):211–215.
12. Choi KY, Liu G, Lee S, Chen X (2012) Theranostic nanoplatforms for simultaneous cancer imaging and therapy: Current approaches and future perspectives. *Nanoscale* 4(2):330–342.
13. Frangioni JV (2003) *In vivo* near-infrared fluorescence imaging. *Curr Opin Chem Biol* 7(5):626–634.
14. Wu C, Chiu DT (2013) Highly fluorescent semiconducting polymer dots for biology and medicine. *Angew Chem Int Ed Engl* 52(11):3086–3109.
15. Zhu X, et al. (2015) Long-circulating siRNA nanoparticles for validating Prohibitin1-targeted non-small cell lung cancer treatment. *Proc Natl Acad Sci USA* 112(25):7779–7784.
16. Gilleron J, et al. (2013) Image-based analysis of lipid nanoparticle-mediated siRNA delivery, intracellular trafficking and endosomal escape. *Nat Biotechnol* 31(7):638–646.
17. Doherty GJ, McMahon HT (2009) Mechanisms of endocytosis. *Annu Rev Biochem* 78:857–902.
18. Whitehead KA, Langer R, Anderson DG (2009) Knocking down barriers: Advances in siRNA delivery. *Nat Rev Drug Discov* 8(2):129–138.
19. Matsumura Y, Maeda H (1986) A new concept for macromolecular therapeutics in cancer chemotherapy: Mechanism of tumoritropic accumulation of proteins and the antitumor agent smancs. *Cancer Res* 46(12 Pt 1):6387–6392.
20. Alexis F, Pridgen E, Molnar LK, Farokhzad OC (2008) Factors affecting the clearance and biodistribution of polymeric nanoparticles. *Mol Pharm* 5(4):505–515.
21. Kedmi R, Ben-Arie N, Peer D (2010) The systemic toxicity of positively charged lipid nanoparticles and the role of Toll-like receptor 4 in immune activation. *Biomaterials* 31(26):6867–6875.
22. Sanderson KM, Skinner D, Stein JP (2006) The prognostic and staging value of lymph node dissection in the treatment of invasive bladder cancer. *Nat Clin Pract Urol* 3(9):485–494.
23. Nucera C, et al. (2010) B-Raf(V600E) and thrombospondin-1 promote thyroid cancer progression. *Proc Natl Acad Sci USA* 107(23):10649–10654.
24. Wan PT, et al.; Cancer Genome Project (2004) Mechanism of activation of the RAF-ERK signaling pathway by oncogenic mutations of B-RAF. *Cell* 116(6):855–867.
25. Killion JJ, Radinsky R, Fidler IJ (1998-1999) Orthotopic models are necessary to predict therapy of transplantable tumors in mice. *Cancer Metastasis Rev* 17(3):279–284.
26. Nucera C, et al. (2009) A novel orthotopic mouse model of human anaplastic thyroid carcinoma. *Thyroid* 19(10):1077–1084.
27. Vahrmeijer AL, Hutteman M, van der Vorst JR, van de Velde CJ, Frangioni JV (2013) Image-guided cancer surgery using near-infrared fluorescence. *Nat Rev Clin Oncol* 10(9):507–518.
28. Pinto N, et al. (2014) Genomically driven precision medicine to improve outcomes in anaplastic thyroid cancer. *J Oncol* 2014(2014):936285.
29. Savvides P, et al. (2013) Phase II trial of sorafenib in patients with advanced anaplastic carcinoma of the thyroid. *Thyroid* 23(5):600–604.